



HAL
open science

Short bends using curved mirrors in silicon waveguides for terahertz waves

Mattias Verstuyft, Elias Akiki, Mathias Vanwolleghem, Guillaume Ducournau, Jean-Francois Lampin, Benjamin Walter, Fuanki Bavedila, Édouard Lebouvier, Marc Faucher, Bart Kuyken

► **To cite this version:**

Mattias Verstuyft, Elias Akiki, Mathias Vanwolleghem, Guillaume Ducournau, Jean-Francois Lampin, et al.. Short bends using curved mirrors in silicon waveguides for terahertz waves. *Optics Express*, 2022, 30 (5), pp. 6656-6670. 10.1364/OE.447268. hal-03695019

HAL Id: hal-03695019

<https://hal.science/hal-03695019v1>



Submitted on 16 Jun 2022

HAL is a multi-disciplinary open access archive for the deposit and dissemination of scientific research documents, whether they are published or not. The documents may come from teaching and research institutions in France or abroad, or from public or private research centers.

L'archive ouverte pluridisciplinaire **HAL**, est destinée au dépôt et à la diffusion de documents scientifiques de niveau recherche, publiés ou non, émanant des établissements d'enseignement et de recherche français ou étrangers, des laboratoires publics ou privés.



Short bends using curved mirrors in silicon waveguides for terahertz waves

MATTIAS VERSTUYFT,^{1,*}  ELIAS AKIKI,² MATHIAS VANWOLLEGHEM,²  GUILLAUME DUCOURNAU,² JEAN-FRANÇOIS LAMPIN,² BENJAMIN WALTER,³ FUANKI BAVEDILA,³ ÉDOUARD LÉBOUVIER,³ MARC FAUCHER,² AND BART KUYKEN¹

¹Photonics Research Group, Ghent University, Technologiepark-Zwijnaarde 126, 9052 Ghent, Belgium

²Institut d'Electronique de Micro-Electronique et de Nanotechnologie, CNRS, Université Lille, 59650 Villeneuve d'Ascq, France

³Vmicro SAS, Avenue Poincaré, 59650 Villeneuve d'Ascq, France

*mattias.verstuyft@ugent.be

Abstract: Dielectric waveguides are capable of confining and guiding terahertz waves along sub-wavelength sized structures. A small feature size allows for a denser integration of different photonic components such as modulators, beam-splitters, wavelength (de)multiplexers and more. The integration of components on a small scale requires bending of the waveguides. In this paper we demonstrate a very short silicon 90°-bend, based on total internal reflection on an elliptically curved outer facet and a rounding of the inner corner joining two waveguides, with an average loss of 0.14 dB per bend in the 600-750 GHz range.

© 2022 Optica Publishing Group under the terms of the [Optica Open Access Publishing Agreement](#)

1. Introduction

The field of terahertz photonics has experienced a growing interest these last few decades and new technologies are bridging the so-called terahertz gap [1]. This term referred to the difficulty in creating sources, based either on the principles of electronic multiplication or bandgap-material based lasers, as well as the issues with making sensitive detectors. Recent developments in quantum cascade lasers, fast photomixers among others have allowed for easier exploitation of the terahertz domain. The interest in this field is largely driven by two distinct applications: on one hand wireless telecommunication technologies experience a strong drive for higher data rates where a higher carrier frequency allows for a denser multiplexing of (slightly) different frequencies [2,3]. On the other hand terahertz waves are of specific interest for sensing purposes. These include gas sensors [4], biodetectors [5] (e.g. for bacteria or cancer cells) but also 3D imaging of samples [6]. Both the fields of telecommunication and sensing benefit massively from miniaturisation. This is not only due to the smaller feature size but also because of a higher light-matter interaction due to the higher concentration of electromagnetic power. To further increase compactification, bends form a crucial component. Our waveguide platform consists of a suspended silicon waveguide attached to a support structure, where the guiding mechanism is based purely on the principle of total internal reflection.

In the following section we discuss different waveguide platforms before moving on to the design used in this work.

2. Waveguide platform

This section starts with a discussion on different guiding techniques for terahertz waves from literature. First we discuss two non-integrated solutions. In Ref. [7] polyurthane was used to create antiresonant waveguides, a technique that is often used at smaller wavelengths [8]. This flexible tube features a loss of 20 dB for a 90° bend with a radius of 10 cm. Another solution

is presented in Ref. [9] where parallel metallic plates guide a 225 GHz wave and a modified T-junction is used to couple terahertz waves into one or both of the arms. Lastly we mention a very basic bare metal wire, such as presented in Ref. [10]. Here a metal wire of 0.9 mm diameter supports a terahertz mode with low loss (0.13 dB/cm for 1 THz), though the modal area is much larger, being a few mm. This also makes the propagation more dependent on environmental effects, such as water vapor absorption.

Integrated waveguide platforms offer the possibility to guide and manipulate electromagnetic waves on scales comparable or smaller than their wavelength. The most common waveguides can be categorized into dielectric platforms and those incorporating metal. In a dielectric waveguide the guiding is based on the principle of total internal reflection where a high index material (n_1) is surrounded by one of lower index (n_2). The platform presented below will simply have silicon at its core ($n_1 = 3.4174$), surrounded by air ($n_2 = 1$). This of course means that the structure will need to be tethered to a supporting structure as we will explain later in this section. It should be noted that silicon used for terahertz guiding is usually of high purity, so-called high resistivity silicon, because the presence of free carriers increase terahertz absorption [11]. This can be achieved by using float-zone melting of a silicon ingot [12]. In Ref. [13] they start from a silicon wafer and etch small holes periodically. Because the hole size is much smaller than the reduced wavelength, this will act as a material with a refractive index in between that of silicon and air. The guiding channel is formed by the absence of the holes in a straight line, a solid section of silicon. Using very high-resistivity silicon (>20 k Ω .cm) they achieved losses of 0.05 dB/cm for the 260-420 GHz range. According to their simulations this platform could support a bend of 2 mm radius with 0.1 dB of loss for frequencies between 260 and 310 GHz. In Ref. [14] a rectangular silicon block is separated from a silicon slab by a thin (2 μ m) SiO₂ layer, which is responsible for much of the absorption. They reported 60° bending losses between 1-4 dB loss (760-920 GHz) for a radius of 3.1 mm. In Ref. [15] an all-silicon rib-waveguide was designed and measurements losses below 1 dB/cm were reported. A sub-class of dielectric waveguides uses photonic crystals. A periodic structure is etched in the same slab as the waveguide which forms a structure with a band gap: allowing some frequencies to propagate while reflecting others. To confine the mode in the vertical direction (perpendicular to the chip-plane) simple total internal reflection between n_1 and n_2 is used. In Ref. [11] and Ref. [16] they opted for silicon and air. They used a triangular lattice and made 60° bends with losses of 0.2 dB and 0.1 dB respectively. The bandwidth is more narrow than other dielectric solutions: roughly 20 GHz in Ref. [11] and 30 GHz in Ref. [16]. In [17] a rectangular lattice was proposed which allows for 90° bends. We have already discussed metal guiding platforms of macroscopic scales. Integrated solutions incorporating metal are often plasmonics based [18]. Two 3D printed plastic wires were covered with silver in Ref. [19]. They fabricated a bend of 2 cm, having a loss of 3 dB. In Sec. 4. we also discuss the structure presented in Ref. [20] where a plasmon wave is excited on-chip to allow for a very short bend.

In this work we opted for a simple dielectric waveguide which is unclad and hence surrounded by air. The main appeal of this approach is the very high index contrast ($n_1 = 3.42$, $n_2 = 1.0$), which allows for a high confinement of the mode, leading in turn to small waveguides and manipulation on a smaller scale. This is done by suspending the structure using anchors tethered to a supporting structure, as can be seen schematically in Fig. 1. From previous devices we concluded that anchors with a width of 15 μ m and length of at least 500 μ m have a negligible effect on the propagating mode [21]. We positioned 5 anchors on both ends with a period of 45 μ m. Since only TE polarized light was used throughout this work, we plot the two supported TE modes at 650 GHz in Fig. 2. Due to the dimensions of the waveguide (210 \times 90 μ m²), as well as the high index contrast, the fundamental mode is highly confined: 92% of the mode is confined in the high-resistivity silicon for a frequency of 650 GHz, which corresponds to a modal area of $0.07\lambda_0^2$. This high confinement limits the parasitic effect of the supporting tethers, though

it comes at the cost of the presence of a higher order TE-mode (Fig. 2, right). This mode will however leak away into the surrounding support structure due to its lower confinement. It can also not be excited by our external source due to the asymmetry of the x component of the electric field, though an asymmetrical structure such as a bend can excite the higher order mode. Using Lumerical 3D FDTD (finite difference time domain) simulations we find however that we can taper from a width of $210\ \mu\text{m}$ to $150\ \mu\text{m}$, the latter forming a single mode waveguide, with a low cost in length and loss. When using a simple trapezoidal taper of $300\ \mu\text{m}$ length the higher order mode will radiate away and the fundamental mode will experience a loss of $0.025\ \text{dB}$ (assuming the material absorption extracted in Sec. 7.). In the next section we expand on the inverted tapers which are used to couple light efficiently from a hollow metallic waveguide (the outputs of our Vector Network Analyzer source) into the waveguide.

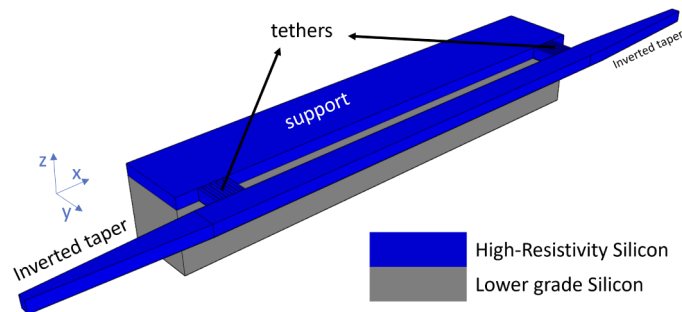


Fig. 1. The waveguide platform: the device layer (blue) is high-resistivity silicon ($\rho > 10\text{k}\ \Omega\cdot\text{cm}$), whereas the handle layer (grey) is regular-grade silicon. 5 anchors ($15\ \mu\text{m}$ wide, $500\ \mu\text{m}$ long and a period of $45\ \mu\text{m}$) on each end tether the waveguide to the surrounding support structure. At the end inverted tapers allow for coupling with modes in hollow metallic waveguides by inserting the taper into them (see Fig. 3).

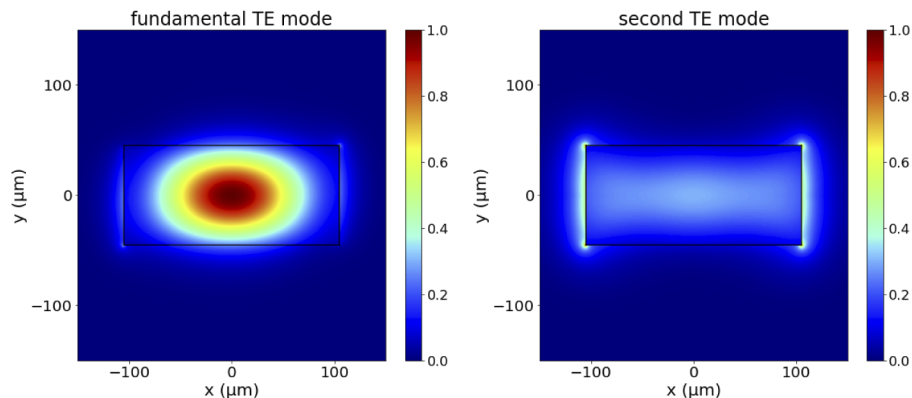


Fig. 2. The electric field intensity for the two guided TE modes for a silicon waveguide ($210 \times 90\ \mu\text{m}^2$) at $650\ \text{GHz}$. The intensity of both is of course symmetric, though the E_x field of the second TE mode (not shown) is antisymmetric. These modes were simulated using Lumerical's 2D finite element eigenmode solver.

3. Inverted tapers

Before we discuss bends, we describe the method by which light is coupled in and out of the silicon waveguides. Hollow metallic waveguides (HMWG, often called rectangular waveguides

in the mm-wave domain) coupled to a vector network analyzer (VNA) were used as the source. The modes in the silicon waveguide and the HMWG have very different mode sizes due to the high refractive index of silicon. Inverted tapers in silicon can enlarge the mode (and lower the effective index), increasing the overlap with the HMWG mode. To further increase the coupling, we insert the inverted taper into the HMWG, as shown in Fig. 3. This technique is also used in Ref. [11]. The taper is 3 mm long and reduces the waveguide width linearly from $210\ \mu\text{m}$ to $66\ \mu\text{m}$ at the edge. We insert the taper by 1 mm into the metallic waveguide. In Fig. 4 the influence of the position of the taper tip on the coupling efficiency and reflections are considered by simulating the coupling using 3D FDTD software (Lumerical). Here the HMWG is modelled as a perfect electrical conductor, while in reality it is made of aluminium which introduces extra losses. Horizontal (y-axis) misalignment will not result in an excitation of the higher order mode (Fig. 2) because the waveguide's width at 1 mm insertion is single mode and does not support that mode. The alignment is performed by using translation stages. What is not shown in Fig. 4 is the reflection, the same simulations show that this fluctuates between -13 and -9 dB for all positions considered.

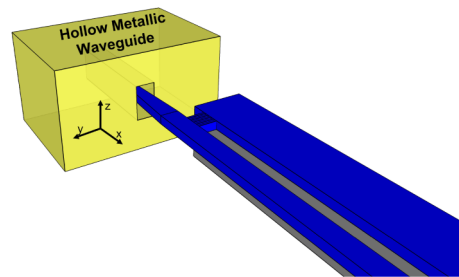


Fig. 3. The hollow metallic waveguide (gold) is coupled to the VNA and the waveguide mode is excited by inserting an inverted taper (blue) into it, allowing for an adiabatic transition into the fundamental waveguide mode.

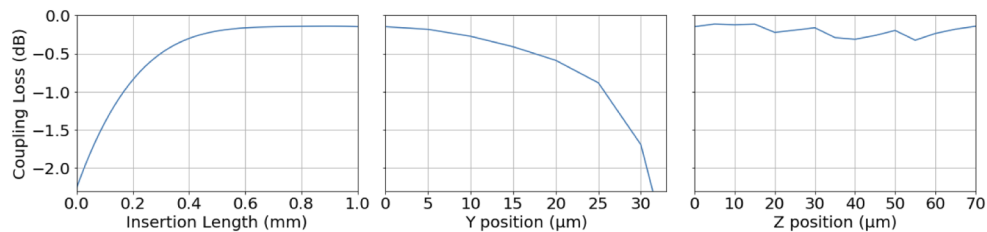


Fig. 4. 3D FDTD simulation results (using Lumerical) investigating the transmission in function of the position of the taper tip for 650 GHz. On the left side the influence of the insertion length is shown. In the middle, the influence of horizontal misalignment is considered for an insertion length of 1 mm. On the right the (minimal) influence of the vertical position is investigated. The most important parameter is obviously the insertion. To ensure reproducibility we always insert the tapers by 1 mm. The other positions are optimized using active alignment. According to these simulations the insertion loss can be as low as -0.15 dB.

Before moving on to the presented structure we first discuss the naive circular bend and the losses associated with it. We then move on to discuss some different solutions from literature, before moving on to our own design. It should be noted that most of the theory used to analyze bends (based on the coupling of modes in different sections) cannot be used for our structure and we need to rely fully on 3D simulations, for which we used Lumerical's FDTD software.

4. Waveguide bends

We start this section by discussing some different options for turning a waveguide mode. We have already discussed a few in the previous section, including non-integrated solutions [7,9] and photonic crystal based solutions [11,16]. We will discuss a few concepts that are compatible with our all-silicon design, but first we mention an interesting hybrid plasmonic-dielectric solution presented in Ref. [20]. Here a silicon waveguide mode excites a plasmonic slot mode that is perpendicular to the original one. Adding again a silicon waveguide, parallel to the original one, allows for two consecutive 90° bends. This allows a waveguide to fold back in on itself or to be laterally shifted. The loss is dependent on the length of the metal slot connecting both silicon waveguides with a high plasmonic propagation loss of 2.5 dB/μm for a wavelength of 1550 nm. More information about this dielectric-plasmonic coupling scheme can be found in Ref. [22]. We go on to discuss different schemes for simple rectangular dielectric waveguides. To understand the need for these we first discuss the loss associated with a simple quarter-circle bend of radius R connecting two perpendicular waveguides, using our waveguide platform: high resistivity silicon with a width of 210 μm and height of 90 μm. The fundamental mode of the straight waveguide is found using the finite difference eigenmode (FDE) solver in Lumerical (employing perfectly matched layer boundary conditions on all sides). This FDE solver also allows one to determine the supported waveguide modes in the bent section. This can be done by using conformal transformations of the space. Upon transforming the solution back to regular (x, y, z) space, the propagation constant will receive an imaginary component [23,24]. The fundamental modes in the straight and bent sections are shown in Fig. 5 for an illustrative bending radius of 600 μm. The loss associated with the bend can be separated into three parts: on one hand there is intrinsic material loss, which is similar to that of the straight waveguide. Another source is due to the mismatch of the mode profile between both modes in Fig. 5. Lastly there is radiation loss, which is due to terahertz waves leaking out of the waveguide. We can determine these from simulations as the conformal transformation converting the bend into a two-dimensional problem results in an imaginary part of the propagation constant β which is to be understood as propagation loss (combination of radiation loss and material absorption). We will now discuss the different sources of loss in function of the bending radius.

- Radiation Loss

The shorter the bending radius is, the larger the angle between the straight waveguide and the walls of the bending section. Unsurprisingly the radiation loss decreases with increasing radius, as evidenced in Fig. 6 (left). Note that these losses are very low compared to the other sources of loss considered below. Furthermore it quickly converges to almost zero radiation loss, the x-axis is much shorter than that of the other figures in Fig. 6. The radiation loss is dependent on the lateral index contrast. In Ref. [25] they increased this for a rib waveguide by performing a full etch in the bending section.

- Mode Mismatch

The different spatial profile between the supported modes in the straight and bent section will result in transmission loss. The higher the bending radius, the more the bent waveguide approaches a straight one, which is why we find again the loss decreasing with increasing radius, as shown in Fig. 6 (middle).

- Propagation Loss

The propagation loss is intrinsic to the material used and little can be done to avoid this through design. There is a linear relation between the path length and the propagation loss, shown in Fig. 6 (right). Minimizing the total propagation loss simply boils down to limiting the size of the bend. To model the loss we used an imaginary refractive index

$\kappa_{Si} = 2.07 \times 10^{-4}$, which is deduced from the linear propagation loss in straight waveguide sections (0.27 dB/cm) measured in Sec. 7.

We see that the radiation and coupling loss decrease with increasing radius, while the opposite is true for the silicon absorption, meaning that there is an ideal radius with minimal loss. According to simulations the ideal bending radius (assuming the value of $\kappa_{Si} = 2.07 \times 10^{-4}$ deduced in Sec. 7.) is 1.877 mm, giving a loss of -0.12 dB.

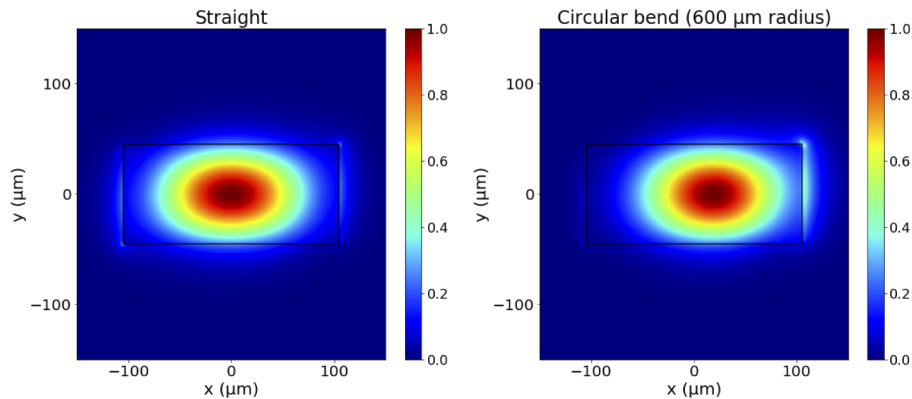


Fig. 5. A comparison of the fundamental mode at 650 GHz in a straight section of the waveguide and the one in a section with constant curvature (radius of 600 μm). The rotational center of the bend is found to the left of the waveguide and hence the mode profiles is pushed to the right compared to the straight waveguide mode. The difference between both profile is one source of loss. The other reasons are material absorption and radiation loss. The latter of these is very low in our wide waveguides. These modes were simulated using Lumerical's 2D finite elements eigenmode solver.

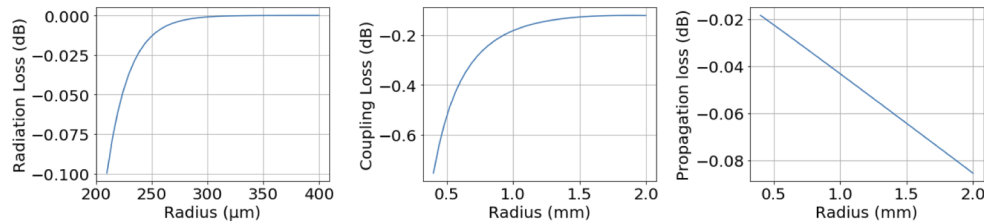


Fig. 6. The losses associated with a simple quarter circle bend in function of the wavelength. Left we see the radiation loss, which is only significant for very short bends (note the different values for the x-axis). In the middle we plot the loss associated with the mode mismatch between the modes in the straight and bent section. On the right is the propagation loss due to material absorption ($\kappa_{Si} = 2.07 \times 10^{-4}$) for the whole bending section. This data was extracted from 2D finite difference eigenmode simulations by Lumerical for a frequency of 650 GHz.

We will now discuss different schemes, most of these were originally designed for optical wavelengths (more commonly used in integrated photonics) but the same techniques are valid for larger wavelengths. The first one we discuss aims to tackle the mode mismatch by shifting the circular waveguide slightly inward by such an amount that the mode overlap is maximal [26]. For telecommunication wavelengths this can be an issue because it requires very precise fabrication [27]. This is less of an issue with the much larger terahertz waves and larger waveguides. Another way to achieve the same goal is to use adiabatic bends as in Ref. [27]. Here a spline is used to

more smoothly increase the curvature of the bending structure, minimizing coupling loss. These splines are quite large however and a certain length penalty is present, which will be discussed in detail in Sec. 5. In Ref. [28] they used a combination of two Euler bends connecting the waveguides to a circular section that only describes a fraction of the total angle and hence has only a fraction of the radiation loss of a regular quarter-circle bend. In this way they make a compromise between the radiation loss and the loss associated with the mode mismatch. In Ref. [29] a sinusoidal section is used in combination with a circular section, again in an effort to balance mode mismatch and radiation loss. Lastly a novel technique was used in Ref. [30] where they used a relatively sharp bend for a wide multimode waveguide and then define pixels (of a predetermined size) in the waveguide that are etched. The amount of etched pixels and their position follows from an optimization algorithm and simulation results. It should be noted that one can't apply semi-analytical techniques as were used to determine the loss of the naive circular bend. Instead one has to rely fully on 3D simulations. This is also true for our bends which should not be modelled as having a propagating mode, which is why we can also call it corners. Instead its performance has to be simulated in 3D (we used Lumerical's FDTD software) where the straight waveguide mode is launched into the corner and the resulting transmission (into the fundamental mode) is recorded after the corner. Note that this is also true for our design which is closer to a reflecting facet (or corner) than a gradual bending of the waveguide.

5. Elliptically curved facet based bends

In the previous section we discussed methods of minimizing losses in rectangular dielectric waveguides bends. These relied on minimizing abrupt mode profile and radiation loss of a bent waveguide mode. However, the bend, or corner, presented here does not rely on a propagating mode in the bending section. Instead it can be understood as a mirror which reflects the waves coming in from the straight waveguide section into the outgoing waveguide. The mode propagation for both a circular bend as the one using an elliptical facet are shown in Fig. 7. The latter is similar to the corners used in Ref. [31], where an angled facet allows coupling from one waveguide to another at a minimal distance, with a loss below 0.18 dB. To improve upon this principle we used the same concept as in Ref. [32]. The geometry is explained in Fig. 8. The facet is replaced by an ellipse section defined by focal points located in the center of the in and outgoing waveguides, separated at a distance of $2p$. This shape increases the amount of terahertz waves which will be reflected at the outer edge by total internal reflection. The ellipse is shifted along the bisector of the two waveguides over a distance of s to account for the Goos-Hänchen effect [33]. Lastly the inner corner is also rounded, circularly this time, with a radius of f .

Now we have three parameters describing the structure. Since this structure cannot be understood using the same analysis used for most bends discussed in Sec. 4, we have to rely on 3D simulations using Lumerical's FDTD (finite-difference time-domain) software to explore the (p, s, f) parameter space. The optimal parameter combination was found to be $(p, s, f) = (250, 30, 250)$ μm . In Fig. 9 we show the simulated transmission loss for a frequency of 650 GHz through different structures, each time keeping one of the parameters constant. Not all combinations of (p, s, f) result in an intersection between the ellipse and the waveguides, which is why some combinations are absent from the plots. A material absorption of $\kappa_{Si} = 2.07 \times 10^{-4}$ was used, extracted from the measurement results in Sec. 7. Since we are only interested in the loss within the corner, we model the straight waveguides as being lossless in the simulations. The resulting loss for the optimal parameters is -0.040 dB. We compare this design with the naive circular bend and the spline bend concept explained in Ref. [27], in function of their size, in Fig. 10. The black dashed line represents the simulated transmission for our design (-0.040 dB). We see that both designs are more lossy at all sizes (though it should be noted that this is dependent on the material absorption). For the full spline we find an optimal transmission of

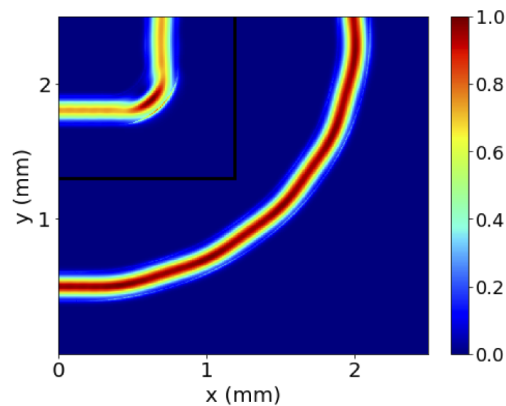


Fig. 7. Two 3D FDTD simulations (Lumerical) comparing the size of the short bend presented here versus a conventional bend with similar loss ($R=2$ mm) at 650 GHz. A small fluctuation of the mode intensity in the outgoing waveguide and in the circular bend can be seen, due to excitation of the second TE mode. For the circular bend the mode conversion is -24 dB and for the facet we find -27 dB. When discussing the transmission only the fraction coupled into the fundamental mode is considered.

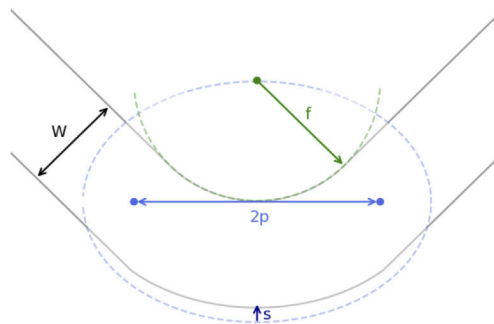


Fig. 8. Top view of the bend structure. An elliptical reflection facet whose focal points are in the center of the waveguides (width $W=210$ μm) at a distance $p=250$ μm from their bisector and a subsequent perpendicular offset $s=30$ μm as well as a rounded inner corner with radius $f=250$ μm .

-0.11 dB for a length of 1.945 mm. For the quarter circle this is -0.12 dB for a radius of 1.877 mm.

In Fig. 7 a small fluctuation of the electric field can be seen in the outgoing waveguide of both designs, as well as within the circular bend. This is due to the excitation of the second TE mode (Fig. 2 (right)). For the elliptical facet we have concluded, from 3D FDTD simulations (Lumerical), that the mode conversion from the fundamental into the second TE mode is -27 dB. For the simple circular bend we found -24 dB of mode conversion. As mentioned in Sec. 2, we can completely get rid of the higher order mode by tapering down to a single mode waveguide width (150 μm). This design is optimized for TE polarized terahertz waves and performs significantly worse for TM modes (-1.2 dB/bend). The main advantage of this bend is its small size. In Fig. 11 we see the three structures pictured together. The gain in chip space consists of two elements: On one hand we have the so-called edge length gained, which we define as the difference in length of the bend section. In Fig. 11 this is shown for one of the arms of the bend, the total edge length gained is twice this value. The other benefit is slightly less obvious and

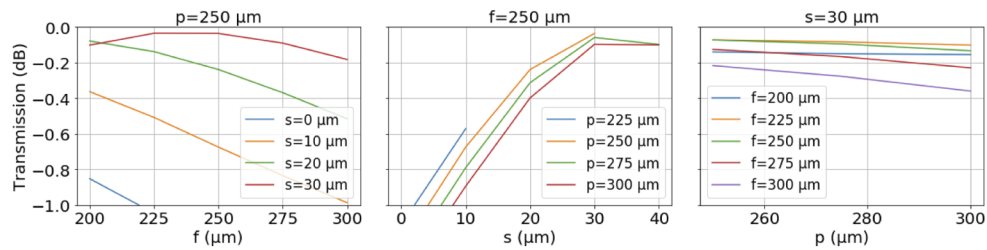


Fig. 9. The 3D FDTD (Lumerical) simulation results of the transmission through the total internal reflection based bend in function of the parameters describing the structure (see Fig. 8). Left: keeping $p=250 \mu\text{m}$ constant. Middle: keeping $f=250 \mu\text{m}$ constant. Right: keeping $s=30 \mu\text{m}$ constant. It should be noted that not every combination of (p, s, f) results in a valid structure. The optimal value is found for $(p, s, f)=(250,30,250) \mu\text{m}$, resulting in a theoretical loss of -0.040 dB per bend.

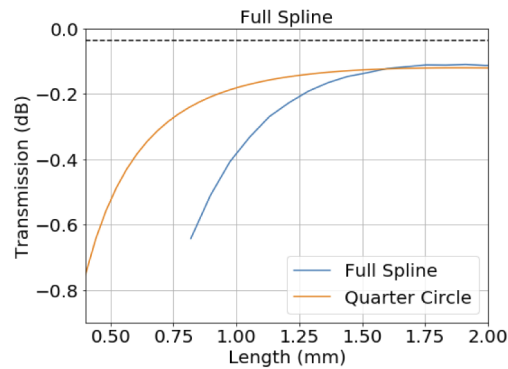


Fig. 10. 3D FDTD simulation (Lumerical) results of the transmission of the fundamental waveguide mode (Fig. 2(left)) through either a bend defined by a full spline (as in Ref. [27]) and the simple quarter circle design in function of their size. For the latter the size is defined as the radius whereas for the former we use the device length L , as defined in Ref. [27]. The black dashed line represents the simulated loss of our design (-0.040 dB). For the material absorption we used $\kappa_{Si} = 2.07 \times 10^{-4}$.

is related to the way chip layout is usually done. As explained in Ref. [27], it is very common for photonic components to need to be routed at a certain distance around another object to minimize evanescent tail coupling. This distance depends on the specific structures considered. Here we have used the same length as the anchors, as their length was determined for the same reason of minimizing evanescent coupling to the support structure (Fig. 1). Depending on the design used for the bends, the waveguides will need to be placed at an according horizontal distance (x) to the object. We call the difference between these positions the offset gained. Compared to the quarter circle, our elliptical facet results in a total edge length gain of 2.3 mm ($2 \times 1.15 \text{ mm}$) and an offset gain of $373 \mu\text{m}$. Compared to the elliptical facet one can see in Fig. 11 that the offset gained is smaller, being $66 \mu\text{m}$, while the edge length gained is longer: 3.0 mm ($2 \times 1.5 \text{ mm}$).

In Fig. 12 we plot the transmission in function of the terahertz frequency. Though this bend was optimized for 650 GHz we see that the loss stays below 0.15 dB per bend for the frequency range $600\text{-}750 \text{ GHz}$.

In the next section we discuss the measurement results. We will see that these deviate from our simulation results by having an extra loss of 0.1 dB , presumably due to fabrication imperfections.

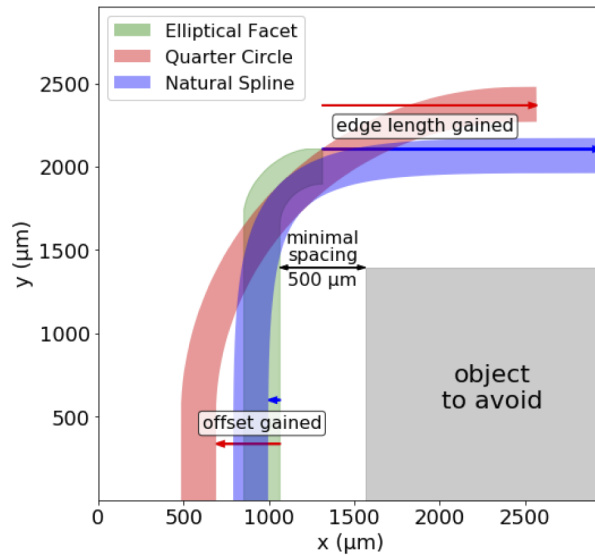


Fig. 11. A comparison of the space needed for our elliptical facet compared to the two simulated optimal designs for a simple circular bend (-0.12 dB) and a full spline bend (-0.11 dB). The edge length gained is (twice) the difference in the length of the arms of the bend. The offset gained refers to the amount of space gained when needing to route around another object. Here a distance of $500 \mu\text{m}$ is used, equal to the anchor length (Fig. 1).

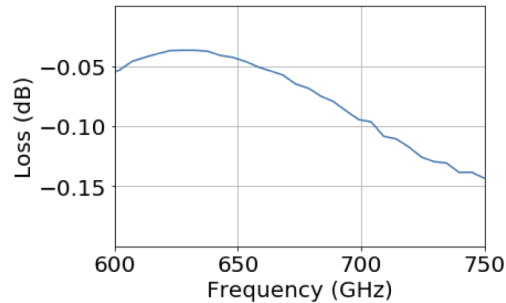


Fig. 12. The transmission spectrum, obtained with 3D FDTD (Lumerical) simulations, through one bend defined by $(p, s, f)=(250,30,250) \mu\text{m}$. The bend performs the best for a frequency around 630 GHz but remains below 0.15 dB for the frequency range 600-750 GHz.

6. Fabrication

In this section we explain how our structures are fabricated by Vmicro SAS. We start from a custom made silicon-on-insulator wafer (provided by Topsil Global Wafers A/S, Fig. 13(a)) where the device layer is $90 \mu\text{m}$ thick silicon of high resistivity ($\rho > 10 \text{ k}\Omega\cdot\text{cm}$) to limit the THz absorption. The handle part underneath the buried silicon dioxide ($2 \mu\text{m}$ thick) is ordinary silicon ($\rho = 10\text{-}20 \Omega\cdot\text{cm}$) that only serves as a support for the suspended waveguide. The waveguide as well as the tethers are etched together by patterning photoresist with UV light (Fig. 13(b)) and employing the Bosch process [34] for deep reactive ion etching (Fig. 13(c)), a technique that allows for good verticality of the sidewalls. The same technique is applied to the backside (Fig. 13(d)) where a much deeper etch is needed. Finally the waveguide is released by wet-etching the silicon oxide away with HF (Fig. 13(e)), resulting in the structure shown in Fig. 13(f).

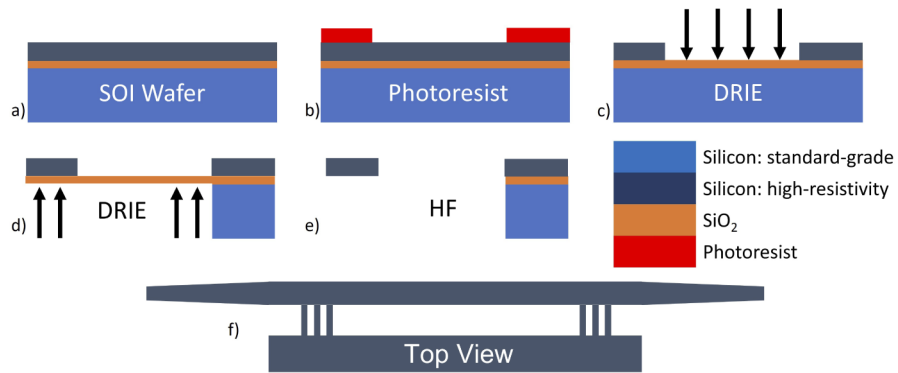


Fig. 13. The fabrication process of the device. Starting from an SOI wafer (a) the waveguides and tethers are defined by patterning a photoresistive material (b) and employing deep reactive ion etching (DRIE, c). To release the waveguide a similar DRIE is applied to the backside (d) after which the oxide layer is removed by a dip in HF (e). A top view schematic is shown in (f).

7. Results

The setup consisted of a 2-port vector network analyzer outputting a TM₀₀ terahertz mode into a hollow metallic waveguide (HMWG). The direction of the polarization has to be twisted using a polarization rotator. One of the VNA ports is fixed, while the other and the sample rest on two movable stages. First one tip of the sample is inserted by 1 mm into the stationary VNA head. The second port is then positioned over the other taper tip, after which both positions are optimized by maximizing the transmission (active alignment). To do this two magnifying lenses are positioned close to the HMWG outputs. To separate the different contributions to the loss (insertion loss, propagation and bending loss) we designed and measured four different structures with a varying number of bends and lengths. An overview is shown in Table 1.

Table 1. Overview of the 4 different samples with varying number of bends and the total length of the straight sections. A third source of loss is the insertion loss which is present for all samples.

Sample name	bends	straight section (mm)
A	0	8
B	4	22
C	12	50
D	20	1

In Fig. 14 a photo of samples B and D is shown. The support part of the chip is glued on top of a piece of epoxy which in turn is attached to a translation stage, allowing for fine active alignment.

First we show the results of a straight waveguide of length 8 mm (Sample A) in Fig. 15. The transmission drops for frequencies below 600 GHz. The waveguide itself supports these lower frequencies but for a taper insertion length of 1 mm the modes are not properly supported inside the taper section. Moreover a dip at 557 GHz can be identified due to water vapor absorption. In the following analysis we will hence limit the discussion to the 600 – 750 GHz frequency range. The transmission spectrum (Fig. 15 (left)) goes up and down (Fabry-Perot interference) due to

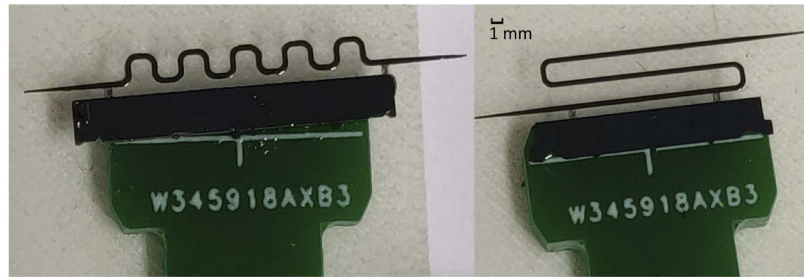


Fig. 14. Pictures of sample B (right) and D (left). Apart from the inverted tapers, waveguide and bends the support part is apparent. This is glued onto a piece of epoxy which can then in turn be attached to a translation stage allowing for fine active alignment. The pictured scale showing the length of 1 mm in the figure is applicable to both images.

reflections at the taper ends (< -10 dB, Fig. 15 (right)). We conclude this from the ratio of the maximal to minimal transmission and the reflection values [35].

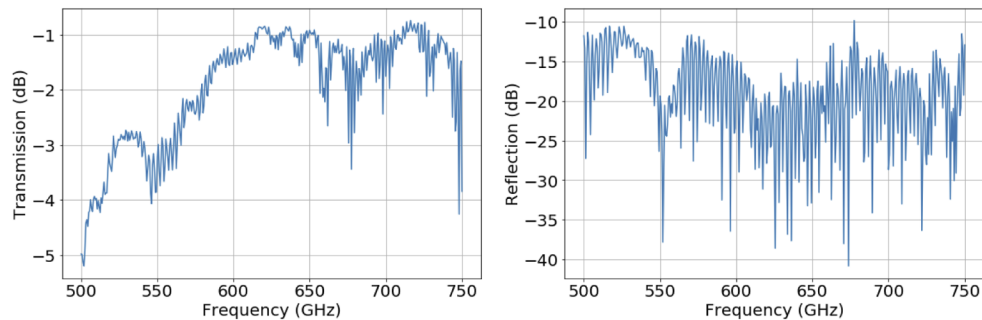


Fig. 15. Measurement results for a straight waveguide (sample A in Table 1) with inverted tapers on both ends (3 mm long, tip width $66 \mu\text{m}$). Left: the transmission (S_{12}). The drop in transmission below 600 GHz is largely due to the inverted tapers: the width of the taper when inserted by 1 mm into the hollow metallic waveguide is insufficient to support low frequency modes. The water vapor absorption line at 557 GHz is also present in this frequency region. The ripples in the transmission are due to Fabry-Perot effects coming from the reflection at the tapers. Right: we see the reflection (S_{22}), staying below -10 dB.

Next we show the transmission of all the different samples in Fig. 16. We see that the ripples are less strong due to extra loss in between the reflections at both ends. A least squares linear regression is performed to determine the three sources of loss: the insertion loss, the propagation loss and the loss per 90° -bend. This is done through the `statmodels` package in python inputting a matrix whose columns are the number of bends, straight section length, the number of tapers (2) for the x-values and the measured loss as the y-value. The results of which are shown in Fig. 17, together with the extracted standard errors. Averaging these out over the 600-750 GHz frequency range results in an average insertion loss and standard deviation of 0.582 ± 0.117 dB per taper, a propagation loss of 0.272 ± 0.006 dB/cm and a loss of 0.141 ± 0.016 dB per 90° -bend. The difference between the simulated and measured transmission spectra are attributed to fabrication imperfections. The mode is essentially reflected at a rough mirror. We have performed a simulation sweep of the imaginary refractive index of the high-resistivity silicon (κ_{Si}) to determine the propagation loss in a straight waveguide section in function of κ_{Si} . This was done using the 2D finite difference eigenmode solver from Lumerical. The measured propagation loss in the straight waveguide sections of 0.27 dB/cm corresponds to $\kappa_{Si} = 2.07 \times 10^{-4}$.

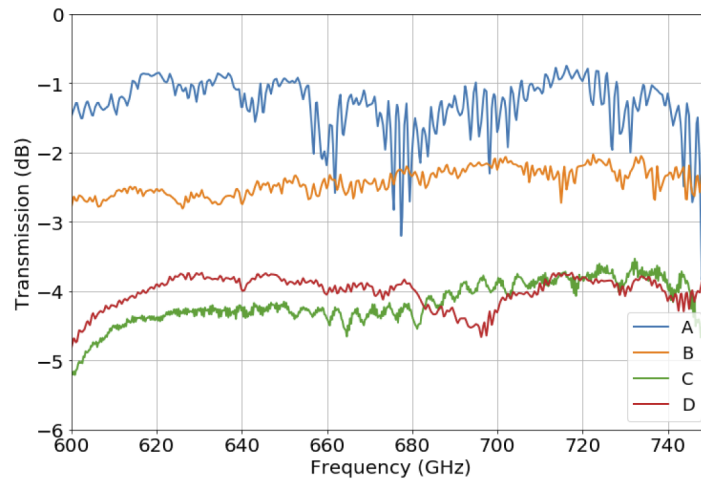


Fig. 16. The measured transmission (S_{12} parameter) for the four structures described in Table 1.

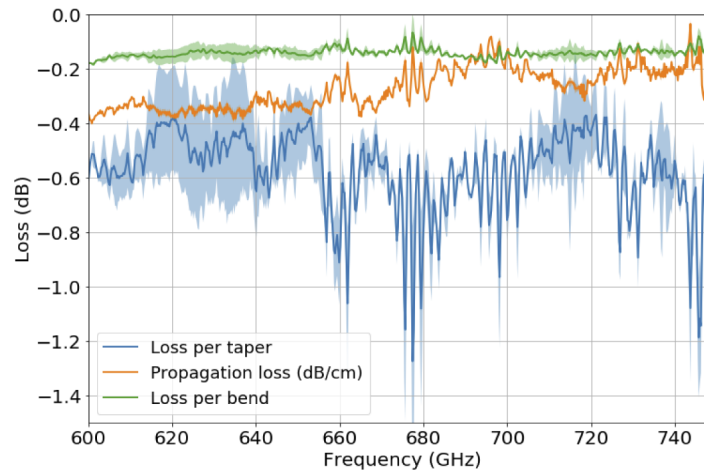


Fig. 17. The three loss parameters extracted using a least squares fit to the data presented in Fig. 16. The average loss in the 600-750 GHz range per taper is 0.58 dB, the propagation loss 0.27 dB/cm and the loss per 90°-bend is 0.14 dB. The standard errors on the loss parameter calculations are shown by the shaded areas.

8. Conclusion

We have demonstrated a short 90°-bend using an elliptical facet and rounded inner corner with an average bending loss of 0.14 dB in the 600-750 GHz frequency range. The platform used features a propagation loss of 0.27 dB/cm and an insertion loss of 0.58 dB.

Funding. Interreg (1.1.11); Fonds Wetenschappelijk Onderzoek (1S32518N).

Acknowledgements. The authors wish to thank the anonymous reviewers for their valuable suggestions.

Disclosures. The authors declare no conflicts of interest.

Data availability. Data underlying the results presented in this paper are not publicly available at this time but may be obtained from the authors upon reasonable request.

References

1. T. Nagatsuma, "Terahertz technologies: Present and future," *IEICE Electron. Express* **8**(14), 1127–1142 (2011).
2. P. Komorowski, P. Czerwińska, M. Kaluza, M. Surma, P. Zagrajek, A. Sobczyk, W. Ciurapiński, R. Piramidowicz, and A. Siemion, "Frequency division multiplexing of terahertz waves realized by diffractive optical elements," *Appl. Sci.* **11**(14), 6246 (2021).
3. T. Nagatsuma, G. Ducournau, and C. C. Renaud, "Advances in terahertz communications accelerated by photonics," *Nat. Photonics* **10**(6), 371–379 (2016).
4. C. F. Neese, I. R. Medvedev, G. M. Plummer, A. J. Frank, C. D. Ball, and F. C. De Lucia, "Compact submillimeter/terahertz gas sensor with efficient gas collection, preconcentration, and ppt sensitivity," *IEEE Sens. J.* **12**(8), 2565–2574 (2012).
5. A. Mazhorova, A. Markov, B. Ung, A. Ng, R. Chinnappan, M. Zourob, and M. Skorobogatiy, "Label-free bacteria detection using evanescent mode of a suspended core terahertz fiber," *2012 Conference on Lasers and Electro-Optics, CLEO 2012* **20**, 20675–20683 (2012).
6. X. C. Zhang, Q. Hu, H. Roskos, and P. Haring Bolívar, "Three-dimensional terahertz wave imaging," *Philos. Trans. R. Soc., A* **362**(1815), 283–299 (2004).
7. A. Stefani, J. Henry Skelton, and A. Tuniz, "Bend losses in flexible polyurethane antiresonant terahertz waveguides," *Opt. Express* **29**(18), 28692 (2021).
8. R. F. Cregan, B. J. Mangan, J. C. Knight, T. A. Birks, P. S. J. Russell, P. J. Roberts, and D. C. Allan, "Single-mode photonic band gap guidance of light in air," *Science* **285**(5433), 1537–1539 (1999).
9. K. S. Reichel, R. Mendis, and D. M. Mittleman, "A Broadband Terahertz Waveguide T-Junction Variable Power Splitter," *Sci. Rep.* **6**(1), 28925 (2016).
10. K. Wang and D. M. Mittleman, "Metal wires for terahertz wave guiding," *Nature* **432**(7015), 376–379 (2004).
11. K. Tsuruda, M. Fujita, and T. Nagatsuma, "Extremely low-loss terahertz waveguide based on silicon photonic-crystal slab," *Opt. Express* **23**(25), 31977 (2015).
12. G. H. Rodway and J. D. Hunt, "Optimizing zone refining," *J. Cryst. Growth* **97**(3-4), 680–688 (1989).
13. W. Gao, X. Yu, M. Fujita, T. Nagatsuma, C. Fumeaux, and W. Withayachumnankul, "Effective-medium-cladded dielectric waveguides for terahertz waves," *Opt. Express* **27**(26), 38721 (2019).
14. H. T. Zhu, Q. Xue, J. N. Hui, and S. W. Pang, "Design, Fabrication, and Measurement of the Low-Loss SOI-Based Dielectric Microstrip Line and its Components," *IEEE Trans. Terahertz Sci. Technol.* **6**(5), 1–10 (2016).
15. B. Kuyken, A. Pagies, M. Vanwolleghem, D. Yarekha, J.-F. Lampin, and G. Roelkens, "Low loss silicon waveguides for the terahertz spectral region," in *2015 40th International Conference on Infrared, Millimeter, and Terahertz waves (IRMMW-THz)*, (2015), pp. 1.
16. Y. Yang, Y. Yamagami, X. Yu, P. Pitchappa, J. Webber, B. Zhang, M. Fujita, T. Nagatsuma, and R. Singh, "Terahertz topological photonics for on-chip communication," *Nat. Photonics* **14**(7), 446–451 (2020).
17. A. Mekis, J. C. Chen, I. Kurland, S. Fan, P. R. Villeneuve, and J. D. Joannopoulos, "High transmission through sharp bends in photonic crystal waveguides," *Phys. Rev. Lett.* **77**(18), 3787–3790 (1996).
18. T. Otsuji and M. Shur, "Terahertz plasmonics," *IEEE Microw. Mag.* **15**(7), 43–50 (2014).
19. Y. Cao, K. Nallappan, H. Guerboukha, G. Xu, and M. Skorobogatiy, "Additive manufacturing of highly reconfigurable plasmonic circuits for terahertz communications," *Optica* **7**(9), 1112 (2020).
20. C. Lin, H. M. Wong, B. Lau, M. A. Swillam, and A. S. Helmy, "Efficient broadband energy transfer via momentum matching at hybrid junctions of guided-waves," *Appl. Phys. Lett.* **101**(12), 123115 (2012).
21. E. Akiki, M. Verstuyft, B. Kuyken, B. Walter, M. Faucher, J. F. Lampin, G. Ducournau, and M. Vanwolleghem, "High-Q THz Photonic Crystal Cavity on a Low-Loss Suspended Silicon Platform," *IEEE Trans. Terahertz Sci. Technol.* **11**(1), 42–53 (2021).
22. C. Huang, C. M. de Sterke, and A. Tuniz, "Simple model for orthogonal and angled coupling in dielectric-plasmonic waveguides," *Opt. Express* **27**(15), 20444 (2019).
23. M. Heiblum and J. H. Harris, "Analysis of Curved Optical Waveguides by Conformal Transformation," *IEEE J. Quantum Electron.* **11**(2), 75–83 (1975).
24. Z. Han, P. Zhang, and S. I. Bozhevolnyi, "Calculation of bending losses for highly confined modes of optical waveguides with transformation optics," *Opt. Lett.* **38**(11), 1778 (2013).
25. M. Cherchi, S. Ylisen, M. Harjanne, M. Kapulainen, and T. Aalto, "Dramatic size reduction of waveguide bends on a micron-scale silicon photonic platform," *Opt. Express* **21**(15), 17814 (2013).
26. M. K. Smit, E. C. Pennings, and H. Blok, "Normalized approach to the design of low-loss optical waveguide bends," *J. Lightwave Technol.* **11**(11), 1737–1742 (1993).
27. W. Bogaerts and S. K. Selvaraja, "Compact single-mode silicon hybrid rib/strip waveguide with adiabatic bends," *IEEE Photonics J.* **3**(3), 422–432 (2011).
28. F. Vogelbacher, S. Nevlacsil, M. Sagmeister, J. Kraft, K. Unterrainer, and R. Hainberger, "Analysis of silicon nitride partial Euler waveguide bends," *Opt. Express* **27**(22), 31394 (2019).
29. X. Tu, M. Li, J. Jiang, D. Goodwill, P. Dumais, E. Bernier, H. Fu, and D. Geng, "Compact low-loss adiabatic bends in silicon shallow-etched waveguides," *IEEE International Conference on Group IV Photonics GFP 2016-November*, 48–49 (2016).
30. Y. Liu, W. Sun, H. Xie, N. Zhang, K. Xu, Y. Yao, S. Xiao, and Q. Song, "Very sharp adiabatic bends based on an inverse design," *Opt. Lett.* **43**(11), 2482 (2018).

31. Y. Wang and D. Dai, "Multimode silicon photonic waveguide corner-bend," *Opt. Express* **28**(7), 9062 (2020).
32. T. Aalto, M. Harjanne, S. Ylinen, M. Kapulainen, T. Vehmas, and M. Cherchi, "Total internal reflection mirrors with ultra-low losses in 3 μm thick SOI waveguides," in *Silicon Photonics X*, vol. 9367 G. T. Reed and M. R. Watts, eds., International Society for Optics and Photonics (SPIE, 2015), pp. 39–47.
33. D. Dai, L. Liu, and S. He, "Analysis of integrated corner mirrors by using a wide-angle beam propagation method," *Opt. Commun.* **260**(2), 733–740 (2006).
34. F. Laermer and A. Schilp, "Method of anisotropically etching silicon," U.S. patent 5501893A (26 March 1996).
35. M. Casalino, G. Coppola, M. Iodice, I. Rendina, and L. Sirleto, "Critically coupled silicon Fabry-Perot photodetectors based on the internal photoemission effect at 1550 nm," *Opt. Express* **20**(11), 12599 (2012).